











Coupled ptychography and tomography algorithm improves reconstruction of experimental data

MAIK KAHNT,^{1,2,*}  JOHANNES BECHER,⁵  DENNIS BRÜCKNER,^{1,2,3}  YAKUB FAM,⁵  THOMAS SHEPPARD,^{4,5} 
TOBIAS WEISSEBERGER,⁶  FELIX WITTEW, ^{1,2}  JAN-DIERK GRUNWALDT,^{4,5}
WILHELM SCHWIEGER,⁶ AND CHRISTIAN G. SCHROER^{1,2} 

¹Deutsches Elektronen-Synchrotron DESY, Notkestraße 85, 22607 Hamburg, Germany

²Department Physik, Universität Hamburg, Luruper Chaussee 149, 22761 Hamburg, Germany

³Ruhr-University Bochum, Universitätsstr. 150, 44801 Bochum, Germany

⁴Institute of Catalysis Research and Technology, Karlsruhe Institute of Technology, Hermann-von-Helmholtz Platz 1, 76344 Eggenstein-Leopoldshafen, Germany

⁵Institute for Chemical Technology and Polymer Chemistry, Karlsruhe Institute of Technology, Engesserstr. 20, 76131 Karlsruhe, Germany

⁶Institute of Chemical Reaction Engineering, Friedrich-Alexander-University Erlangen-Nürnberg, Egerlandstraße. 3, 91058 Erlangen, Germany

*Corresponding author: maik.kahnt@desy.de

Received 15 July 2019; revised 25 August 2019; accepted 26 August 2019 (Doc. ID 372667); published 26 September 2019

Three-dimensional (3D) x-ray microscopy by ptychographic tomography requires elaborate numerical reconstructions. We describe a coupled ptychography-tomography reconstruction algorithm and apply it to an experimental ptychographic x-ray computed tomography data set of a catalyst particle. Compared to the traditional sequential algorithm, in which ptychographic projections are reconstructed to serve as input for subsequent tomographic reconstruction, the coupled ptychography-tomography algorithm reconstructs the 3D volume with higher spatial resolution over a larger field of view. Coupling the data from different projections improves the overall reconstruction, and the ptychographic sampling in individual projections can be coarsened beyond the point of overlap between neighboring scan points, still leading to stable reconstructions. © 2019 Optical Society of America under the terms of the OSA Open Access Publishing Agreement

<https://doi.org/10.1364/OPTICA.6.001282>

1. INTRODUCTION

Knowing the structure of nanomaterials and nano-objects is key to understanding their properties and function. X rays are an ideal probe to study their three-dimensional (3D) nanostructure. Due to their large penetration depth and short wavelength, x rays make nondestructive 3D imaging at the nanoscale possible. Ptychographic x-ray computed tomography (PXCT) is an emerging microscopy technique that uniquely offers high spatial resolution and sensitivity among contemporary x-ray imaging methods, producing 3D quantitative maps of the complex index of refraction of the sample [1]. In this way, it yields quantitative information on the local electron density. By now, PXCT has been established as a method at multiple synchrotron-radiation facilities around the world [2–8].

A tomographic data set is obtained by recording ptychographic projections of a sample for a set of rotation angles. As of today, to retrieve the volumetric information, first the projections are generated by ptychographic reconstruction. In a second step, following alignment and artifact removal, these projections serve as input for conventional tomographic reconstruction of the sample volume. Recently, it was proposed to couple these two steps of ptychographic and tomographic reconstruction to relax scanning

overlap requirements, to allow for flexible acquisition patterns, and to reduce overall scan times and thus radiation dose to the sample [9]. Various algorithms were proposed to reconstruct the acquired data in one single coupled ptychographic tomography (CPT) step. So far, all of these algorithms were tested solely on numerical model data sets [9–11] or relied on knowing the exact probe function prior to the reconstruction [12]. In this article, a CPT reconstruction is presented and applied to an experimental PXCT data set. The reconstruction is compared to conventional PXCT in terms of resolution and image quality.

2. METHODS

In the classic ptychographic tomography model, the sample is represented by its 3D complex-valued index of refraction,

$$n(\mathbf{r}) = 1 - \delta(\mathbf{r}) - i\beta(\mathbf{r}), \quad (1)$$

where $\mathbf{r} = (r_x, r_y, r_z)$ are coordinates fixed in the frame of the sample, $\delta(\mathbf{r})$ is the refractive index decrement, and $\beta(\mathbf{r})$ is the absorption term. During ptycho-tomographic data acquisition, the sample is scanned in translation through the probing beam along the laboratory-fixed coordinates ρ_x and ρ_y and in rotation around the ρ_y axis by the rotation angle Θ

(see Fig. 1). The transformation matrix \mathbf{R}_Θ between sample coordinates \mathbf{r} and laboratory coordinates $\boldsymbol{\rho}$ is given by

$$\mathbf{r} = \begin{pmatrix} r_x \\ r_y \\ r_z \end{pmatrix} = \begin{pmatrix} \rho_x \cos \Theta - \rho_z \sin \Theta \\ \rho_y \\ \rho_x \sin \Theta + \rho_z \cos \Theta \end{pmatrix} = \mathbf{R}_\Theta \cdot \boldsymbol{\rho}. \quad (2)$$

At each rotation angle Θ , the sample is probed by the wave field $P(\boldsymbol{\rho})$ at multiple discrete lateral shift positions $(q_{x,j}, q_{y,j})$. If the sample is optically thin and multiple scattering can be neglected, the complex wave field behind the sample can be modeled as

$$\Psi_{\Theta,j}(\rho_x, \rho_y) = P(\rho_x, \rho_y) O_\Theta(\rho_x - q_{x,j}, \rho_y - q_{y,j}), \quad (3)$$

where

$$\begin{aligned} O_\Theta(\rho_x, \rho_y) &= \exp \left(ik \cdot \left[1 - \int_{-\infty}^{+\infty} n(\boldsymbol{\rho}) d\rho_z \right] \right) \\ &= \exp \left(i \cdot \underbrace{\left[k \cdot \int \delta(\boldsymbol{\rho}) d\rho_z \right]}_{=\phi(\rho_x, \rho_y)} \right) \exp \left(\underbrace{\left[-k \cdot \int \beta(\boldsymbol{\rho}) d\rho_z \right]}_{=a(\rho_x, \rho_y)} \right) \end{aligned} \quad (4)$$

is the complex transmission function of the object obtained by projection along the ρ_z axis. Here, $k = 2\pi/\lambda$ is the wavenumber of the probing beam, and λ is its wavelength. The phase shift to the probing beam is called $\phi(\rho_x, \rho_y)$ and the logarithmic modulus of the sample $a(\rho_x, \rho_y)$. At each scanning position, the far-field diffraction pattern $I_{\Theta,j}$ is measured, which is the absolute square of the Fourier transform of $\Psi_{\Theta,j}$,

$$I_{\Theta,j}(q_x, q_y) = |\mathcal{F}[\Psi_{\Theta,j}(\rho_x, \rho_y)]|^2. \quad (5)$$

Several algorithms have been developed to solve for the unknown complex object projections $O_\Theta(\rho_x, \rho_y)$ and a set of probes $P_\Theta(\rho_x, \rho_y)$ using the measured diffraction patterns $I_{\Theta,j}(q_x, q_y)$ and relative scan positions $\boldsymbol{q}_{\Theta,j}$ [13–16]. After reconstructing all the projections $O_\Theta(\rho_x, \rho_y)$, they are typically freed of artifacts such as phase wraps and phase wedges. For each projection at a given angle Θ , the relative scan positions $\boldsymbol{q}_{\Theta,j}$ are accurately known. However, due to mechanical inaccuracies of the tomographic scanner under rotation and thermal drifts, the projections

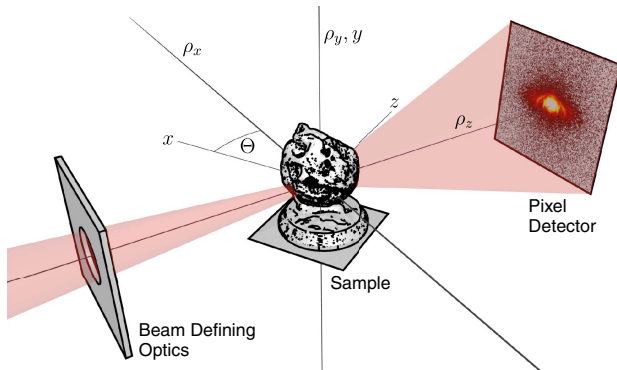


Fig. 1. Geometry for Ptychographic Tomography. To record a projection, the sample is scanned perpendicularly to the probing beam (red) along ρ_x and ρ_y , recording a far-field diffraction pattern at each position of the scan. A tomographic data set is recorded by acquiring a series of projections rotating the sample around the ρ_y axis to multiple angles Θ . The sample is described in the coordinate system $\mathbf{r} = (r_x, r_y, r_z)$ fixed to the frame of the sample. It is rotated by Θ relative to the laboratory coordinate system $\boldsymbol{\rho} = (\rho_x, \rho_y, \rho_z)$.

often need to be aligned relative to each other prior to tomographic reconstruction. Once all projections are aligned to each other, any tomographic algorithm can be used to reconstruct the refractive index $n(\mathbf{r})$ from the aligned projections $O_\Theta(\rho_x, \rho_y)$.

We recorded a Ptychographic Nano-Analytical Microscope (PtyNAMi) at beamline P06 of the synchrotron-radiation source PETRA III at the Deutsches Elektronen-Synchrotron DESY in Hamburg, Germany [17]. The instrument is built for Ptychographic imaging with high spatial resolution [18] and sensitivity [19], as well as with chemical contrast [20]. The sample is a macroporous zeolite particle [21,22] of about 2.6 μm diameter that has prominent features (internal macropore system) of a few 100 nm. It is mostly composed of very porous silica and alumina and can be regarded as weakly scattering. The sample was mounted freestanding on top of an aluminum pin by focused ion beam milling and beam-induced metal deposition [cf. Fig. 2(a)].

The sample was aligned in the x-ray microscope [17] using an optical microscope. The incident 9 keV photon beam was focused to a 70 nm spot using a Fresnel zone plate. The sample was placed 1 mm downstream of the focus, increasing the beam size on the sample to about 1.8 μm full width at half-maximum. For each projection angle Θ , 121 diffraction patterns $I_{\Theta,j}$ (exposure time 1 s) with a size of 256×256 pixels were recorded using an EIGER X 4M detector (DECTRIS, Switzerland), placed 2.13 m downstream of the sample. This results in a pixel size of 16.5 nm in the reconstructions. In this way, a field of view of $4 \times 4 \mu\text{m}^2$ was covered by a rectangular grid of 11×11 positions (step size 400 nm). The relative sample positions were recorded using an interferometer-based sample tracking system. In total, 90 projections were recorded in 2° steps over 180° . The Ptychographic tomography data set consists of $90 \times 121 = 10890$ diffraction patterns. The overall recording time for the whole data set was approximately 7 h.

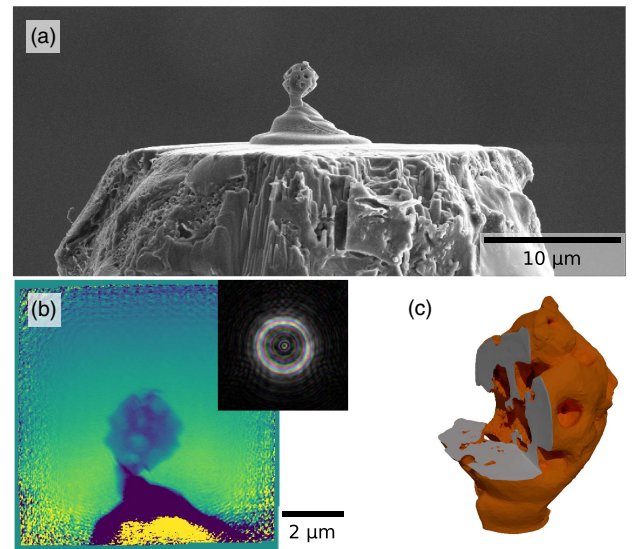


Fig. 2. (a) SEM image of the macroporous zeolite particle, mounted freestanding on top of a platinum pedestal at the tip of an Al pin; (b) phase image of a Ptychographically reconstructed projection $O_\Theta(\rho_x, \rho_y)$ with phase wrap at the bottom of the reconstructed field of view and corresponding reconstructed complex probing wave field $P_\Theta(\rho_x, \rho_y)$; (c) 3D isophase surface rendering of the reconstructed volume $n(\mathbf{r})$ with a cutout to reveal the inner pore structure of the sample.

3. RESULTS

A. Preliminary Reconstruction

As a first step, we reconstructed the first recorded projection on its own using 5000 iterations of the extended Ptychographical Iterative Engine (ePIE) algorithm [15], resulting in an object projection $O(\rho_x, \rho_y)$ and a reconstructed probe function $P(\rho_x, \rho_y)$ [see Fig. 2(b)]. The reconstructed probe function was subsequently used as an initial probe estimate for all upcoming reconstructions. This is sensible, as no PXCT measurement will be performed without having tested the successful reconstruction of a single projection first. Hence, the knowledge of the probe function, or at least a close estimate, can be used to reduce the number of iterations needed for all following projections. The high number of iterations was chosen to make sure the algorithm and therefore the probe estimate had converged properly.

B. PXCT Reconstruction

For the comparison with the coupled Ptychography-tomography reconstruction, we first reconstructed the data using the already

established PXCT framework. Using the initial estimate for the probe function, all 90 recorded projections were reconstructed for 50 iterations with the ePIE algorithm, resulting in 90 complex projection images $O_\Theta(\rho_x, \rho_y)$ and 90 corresponding complex probe functions $P_\Theta(\rho_x, \rho_y)$. Phase wraps and phase wedges were removed from the reconstructed projections before they were aligned to each other (see Supplement 1 for details). The projections were aligned by alternately correlating the plane integral phase profiles perpendicular to the rotation axis and matching the center of mass of the plane integral phase profiles parallel to the rotation axis of all projections [23]. The final tomographic reconstruction of the aligned projections was carried out using 50 iterations of the simultaneous algebraic reconstruction technique (SART) [24,25], as it was also used in the CPT algorithm later on. This way, each diffraction pattern and each projection is used as often in the PXCT reconstruction as it is used in the CPT reconstruction. Two slices of the PXCT reconstructed phase volume are shown in the top row of Fig. 3.

C. CPT Reconstruction

Algorithm 1. Coupled Ptychography and tomography reconstruction of a PXCT data set. This algorithm equals the framework of [9] with M iterations of the ePIE algorithm [15] used as data constraint and the SART algorithm for the object constraint. A detailed description can be found in Supplement 1.

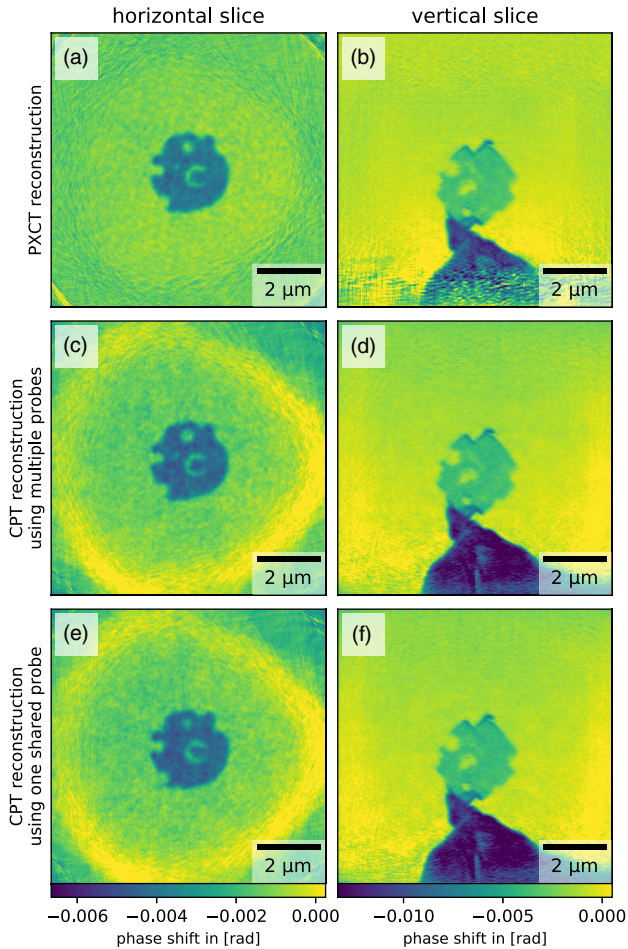


Fig. 3. Comparison of the phase reconstructions $\Phi(\mathbf{r})$ using (a), (b) the standard PXCT framework; (c), (d) the CPT framework using Algorithm 1 and an individual probe for each projection angle; and (e), (f) the CPT framework with one shared probe for all projection angles. All reconstructions were done on a volume of 660^3 voxels, $N = 50$ 3D iterations, $M = 1$ ePIE iteration, and the update strengths $\alpha = 1.0$ for the object, $\beta = 1.0$ for the probing wave fields, and $\gamma = 1.0$ for the volume.

- 1: **procedure** PTYCHOTOMO ($I_u, \mathbf{q}_{\Theta, k}, P_\Theta(\rho_x, \rho_y)$)
- 2: create a 3D array $A(\mathbf{r})$ for the logarithmic modulus and a 3D array $\Phi(\mathbf{r})$ for the phase shift. \triangleright initial entries 0
- 3: **if** no $P_\Theta(\rho_x, \rho_y)$ are given **then**
- 4: initialize appropriate $P_\Theta(\rho_x, \rho_y)$ for each recorded projection angle Θ
- 5: **loop** N times
- 6: **for** every Θ **do**
- 7: calculate the projections $a_\Theta(\rho_x, \rho_y)$ and $\phi_\Theta(\rho_x, \rho_y)$ under the angle Θ
- 8: calculate the complex projection $O_\Theta(\rho_x, \rho_y) = \exp(a_\Theta(\rho_x, \rho_y) + i\phi_\Theta(\rho_x, \rho_y))$
- 9: do M Ptychography iterations on $O_\Theta(\rho_x, \rho_y)$ using $I_{\Theta, j}(u)$, $\mathbf{q}_{\Theta, j}$, and P_Θ to obtain an updated estimate $\hat{O}_\Theta(\rho_x, \rho_y)$ for that projection \triangleright e.g., using the ePIE algorithm
- 10: calculate the logarithmic modulus $\Delta a_\Theta(\rho_x, \rho_y) = \log|\hat{O}_\Theta(\rho_x, \rho_y)| - \log|O_\Theta(\rho_x, \rho_y)|$ and phase shift update $\Delta \phi_\Theta(\rho_x, \rho_y) = \arg(\hat{O}_\Theta(\rho_x, \rho_y)) - \arg(O_\Theta(\rho_x, \rho_y))$
- 11: calculate the 3D logarithmic modulus and phase shift updates $\Delta A_\Theta(\mathbf{r})$ and $\Delta \Phi_\Theta(\mathbf{r})$ by backprojecting $\Delta a_\Theta(\rho_x, \rho_y)$ and $\Delta \phi_\Theta(\rho_x, \rho_y)$ under the angle Θ
- 12: update the object volumes: $A(\mathbf{r}) \leftarrow A(\mathbf{r}) + \gamma \cdot \Delta A_\Theta(\mathbf{r})$ and $\Phi(\mathbf{r}) \leftarrow \Phi(\mathbf{r}) + \gamma \cdot \Delta \Phi_\Theta(\mathbf{r})$ \triangleright update strength $\gamma \in (0, 1]$
- 13: **return** $A(\mathbf{r})$ and $\Phi(\mathbf{r})$.

Using the position shifts determined during the alignment of the PXCT reconstruction, the relative sample positions measured by the interferometers were transformed to absolute positions $\mathbf{q}_{\Theta, j}$ in relation to the shared rotation axis. Algorithm 1 was used to reconstruct the measured data again, but this time by coupling Ptychography and tomography—the so-called CPT method—and not solving them sequentially.

For the first CPT reconstruction, all 90 probes were initialized with the probe reconstructed during the preliminary

reconstruction. This initial guess of the probe function leads to reliable and fast convergence. During the reconstruction, the probe for each projection was refined individually.

The result of the coupled reconstruction [see Figs. 3(c) and 3(d)] matches that of the PXCT reconstruction [see Figs. 3(a) and 3(b)]. It even reconstructs farther down towards the platinum base, where the PXCT reconstruction produces artifacts, since the base is not covered from all projections due to mechanical shifts. In the horizontal slices, a faint halo can be seen around the particle in the center. This halo coincides with the edge of the field of view of the most intense parts of the probing beam from every projection angle Θ .

Choosing $N = 1$, M very large, and $\gamma = 1$ in Algorithm 1 would make the coupled algorithm almost the PXCT algorithm. The difference is that in the PXCT algorithm each projection is reconstructed with an empty initial object, while in the CPT reconstruction each projection starts with the projection of the current state of the reconstructed volume, which would have already been influenced by all previously treated projection angles.

Total variation algorithms [26] could be used on the reconstructed volumes to smoothen the object without blurring the edges and thus increase the quality of the reconstructed volumes [9,11]. As it can be used both on the CPT results and the PXCT after the respective reconstructions, we decided to waive this additional step and compare the unadulterated results of both algorithms to each other.

D. Resolution Comparison

To compare the quality of the CPT reconstruction to the PXCT reconstruction, we estimated and compared spatial resolutions. At first we used the volumes reconstructed from all recorded diffraction patterns [see Figs. 3(a)–3(d)] to extract multiple line profiles across edges in the volume. The profiles were then fitted with an error function. From these fits, the edge widths were extracted as the distance between the 10% and 90% level of the edge. The widths for the PXCT reconstructed volume ranged between 139 and 183 nm, while the widths for the CPT reconstructed volume ranged between 123 and 148 nm (see Supplement 1, Fig. S1). For all profiles, the width of the CPT reconstruction was at least 16.3 nm (approximately one pixel) smaller than the one for the PXCT reconstruction.

To not only evaluate local resolution, we also estimated the resolution using the Fourier shell correlation. To this end, we split the data set into two complementary halves, assigning to each

projection the diffraction patterns alternately to one or the other half (see Supplement 1, Fig. S2).

Each of the two half data sets was then reconstructed independently, once using the PXCT framework and once using Algorithm 1. Both algorithms were run with the same parameters as before. Using Fourier shell correlation on these pairs of volumes and the half-bit threshold, resolutions of 72.5 nm (PXCT) and 65.3 nm (CPT) were estimated [see Fig. 4(a)]. Finally, we also calculated the (spatial) spectral signal-to-noise ratios (SSNRs) using these volumes [see Fig. 4(b)]. These gave us estimates of 76.5 nm (PXCT) and 66.9 nm (CPT) for the achieved resolution. In all cases, the CPT reconstruction achieved the higher resolution.

This modest improvement in resolution using the CPT algorithm is most likely a result of self-alignment of the projections during the 50 iterations of the CPT algorithm. During the alignment step, the PXCT algorithm is limited to aligning the relative positions between the projections, without being able to adapt or improve the projections themselves. The CPT algorithm has more freedom. It can slightly shift probe and object projection by adding a phase wedge to the reconstructed probe function, but it can also improve the projections and possible artifacts in these projections during each iteration. Both algorithms were run using the exact same data, started with the same initial estimate of the probe function for all projections, used each recorded diffraction pattern exactly 50 times to update the projection/volume, and both performed exactly 50 tomographic updates over all projections.

E. CPT with Only One Shared Probe

Using only one probe function $P(\rho_x, \rho_y)$ for all projection angles Θ increases the cross-linking in the Ptycho-tomographic data set even more. This additional coupling not only by the object but also by the probe requires the probe to be unchanged during the whole experiment and not only during the measurement of each single projection. The CPT reconstruction using one common probe $P(\rho_x, \rho_y)$ for all projections is shown in Figs. 3(e)–3(f). This reconstruction is slightly noisier than the CPT reconstruction with multiple probes, but works robustly. This indicates more or less stable experimental conditions over the period of data acquisition. However, there are slight fluctuations in the illumination over time. While the 90 reconstructed probe functions $P_\Theta(\rho_x, \rho_y)$ resemble each other, they have tiny differences due to instabilities of the electron orbit and the

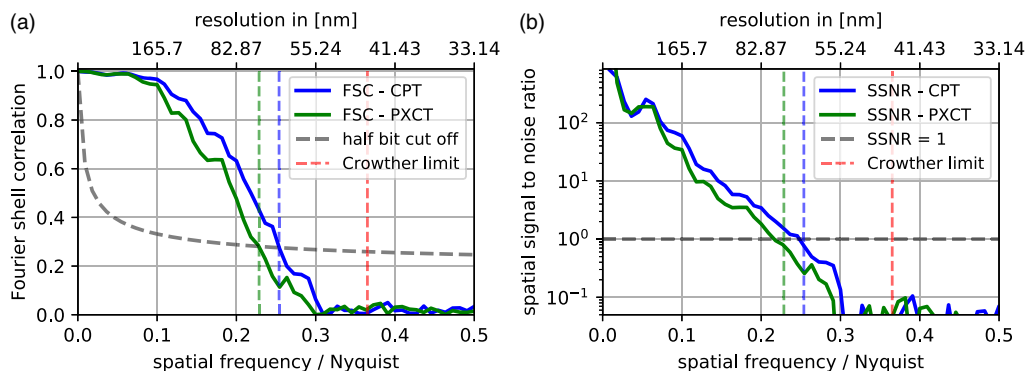


Fig. 4. Resolution estimation for the volumes reconstructed using the PXCT algorithm and the CPT algorithm. (a) Estimation using Fourier shell correlation; (b) estimation using the spatial signal-to-noise ratio.

x-ray optical beamline components over the duration of the experiment. As the shared probe function $P(\rho_x, \rho_y)$ averages over these instabilities, the shared-probe CPT reconstruction cannot adapt to slightly varying experimental conditions and thus cannot optimally fit the data in a real experiment.

PXCT could also be performed using only one shared probe. All projections would have to be reconstructed simultaneously while sharing the same probe function. This is not usually done, as beam instabilities over the duration of PXCT experiments are an issue. Sometimes two consecutive scans, between which the detector was shifted, are reconstructed this way to alleviate artifacts created by gaps between the detector panels, where no information was recorded [2,27,28]. But reconstructing all recorded PXCT projections with one shared probe would only allow the reconstruction of a ground truth of probe function. In the presence of beam instabilities, this would reduce the resolution of the reconstructed projections, resulting in a worse overall resolution in the reconstructed volume. Assuming perfect beam stability, this coupling of the PXCT projection reconstructions via the shared probe function could relax the required sampling. As all projections act on and influence the probe function, some sparser sampled projections could still be reconstructed properly, as the other properly sampled projections always enforce the correct probe function. But the relaxation of the sampling cannot pass the point of no overlap, as no projected object can be reconstructed where the beam never hit. In this regard both CPT methods, with a shared probe or individual probes, surpass the possible PXCT

reconstruction with one shared probe, as they are coupled via the object.

In the presence of long-term beam instabilities, PXCT and CPT with individual probes for each projection allow us to compensate those instabilities to some extent.

F. CPT with Reduced Sampling

For model data, it was shown in [9] that the overlap needed for a successful ptychographic reconstruction can be reduced when performing a CPT reconstruction, as the overlap is given in the tomographic plane. Here, we verified this by removing diffraction patterns from the data set and running the same reconstruction as before. Figure 5 shows the reconstructions if only every n th diffraction pattern ($n = 1, \dots, 5$) in the horizontal direction is used for the PXCT and CPT reconstruction. Even when using only every fifth diffraction pattern, and having neighboring probing beams no longer overlap in the horizontal direction, the object is still reconstructed in both cases. This is most likely a result of the very good initial guess of the probe function used in all reconstructions. As more and more diffraction patterns are skipped, the reconstructions become noisier and noisier. This is directly related to the effectively reduced dose applied to obtain the tomogram.

By comparing the projections reconstructed using the PXCT algorithm and the CPT algorithm in Figs. 5(a)–5(e), it can be seen that the PXCT reconstructions suddenly suffer large artifacts once the point of no-overlap is approached. In practice, these

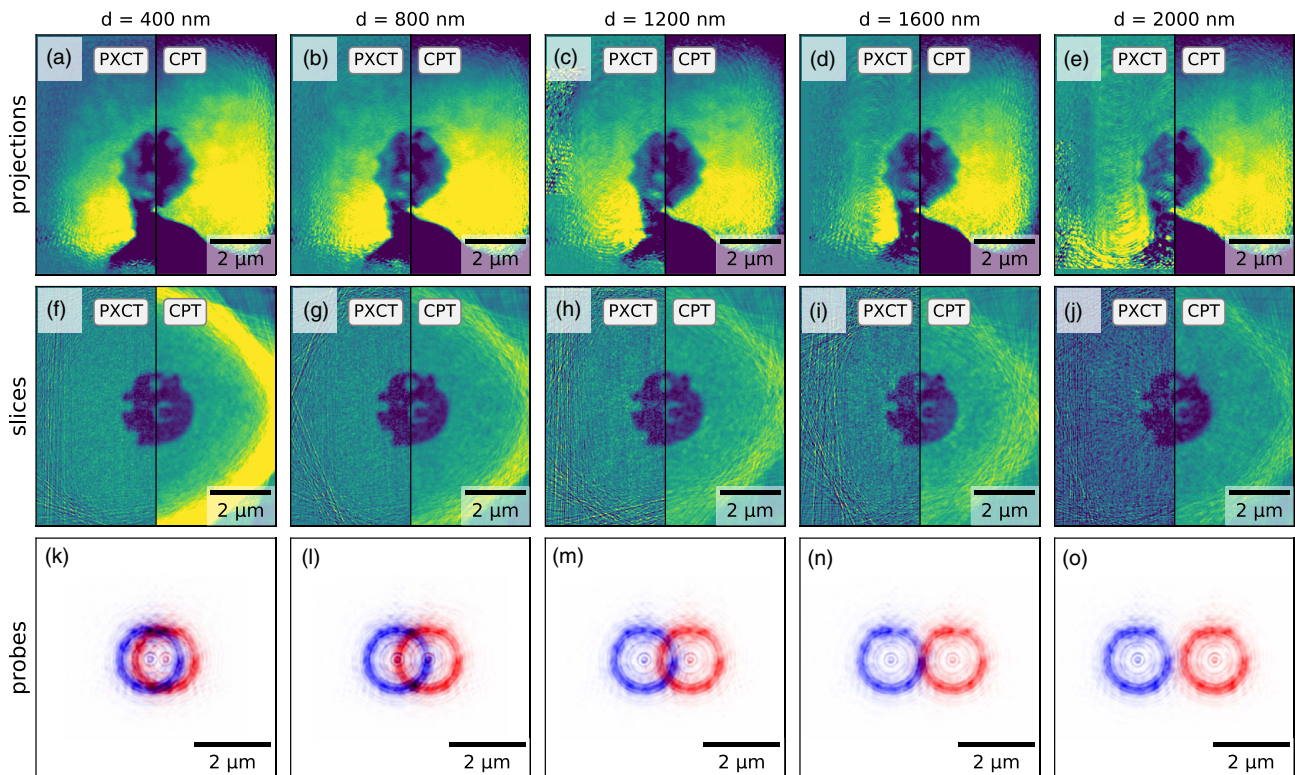


Fig. 5. Reconstructions of the data set when only every n th diffraction pattern in the horizontal direction ($n = 1, \dots, 5$) is used, effectively increasing the horizontal step size from 400 to 2000 nm. (a)–(e) show the reconstructed projections using 100 iterations of the ePIE algorithm (left) against the projection of the volume reconstructed using $N = 100$ iterations of Algorithm 1. The color scale is chosen such that the reconstruction artifacts are highlighted. (f)–(j) show a slice through the reconstructed volume using the PXCT algorithm (left) and the CPT algorithm (right). (k)–(o) show the overlap of the probing beam intensities of two neighboring horizontal positions for each case.

artifacts would complicate the alignment of the reconstructed projections. Here, we assumed all positional parameters to be known and used these projections as input for the SART algorithm for tomographic reconstruction. Slices through the reconstructed volumes are shown in Figs. 5(f)–5(j). With increasing horizontal step size, the noise increases for both algorithms, but the contrast between air and particle shrinks only in the PXCT reconstructions and stays constant in the CPT reconstructions. For the CPT reconstructions, the resolutions were estimated using Fourier shell correlation (see Supplement 1, Figs. S5 and S6), revealing an increasing degradation of the resolution from 65.3 at 400 nm horizontal step size to 114 nm at 2000 nm horizontal step size.

4. DISCUSSION

In this implementation, corrections for projected phase shifts and absorption coefficients are added to the current object estimate sequentially from one projection angle to the next. Therefore, we refer to this tomography algorithm as SART. Various other tomography algorithms [29–31] could be used for this coupled reconstruction, such as the filtered backprojection or the simultaneous iterative reconstruction technique (SIRT) [32,33]. We decided to use the SART implementation, as its essence is the same as the ePIE algorithm: estimate the result, simulate the measurement for one angle, calculate the difference, use the difference to update the current estimate, and repeat this for all other angles. We deemed it the most basic, simplest implementation of a CPT algorithm and implemented it sequentially.

The coupled pycho-tomographic algorithm can be massively parallelized. One possibility is to calculate, update, and backproject all projections at the same time. This would correspond to the SIRT algorithm. Another variant could use parallel pychographic methods to solve the two-dimensional (2D) pychographic problem for each projection instead of the sequential ePIE algorithm [13,34,35]. Instead of going through the scan positions sequentially, the updates can be calculated and applied simultaneously. The prospect for optimization of the CPT process is therefore high.

Instead of parallelizing the reconstruction, more advanced pychography algorithms could also be used to adapt CTP to more complex experimental conditions (for example, to deal with incoherent modes [36], slightly too large probing beams [37] or imperfect scanning positions [38,39]). Other usable algorithms are designed to deal with experimental choices such as performing fly-scans instead of step scans [40–43], using a broader bandwidth for more flux [44,45] or even performing near-field pychography [4]. Total variation steps [26] could also be incorporated into the CPT algorithm. Instead of performing the total variation refinement at the end of the CPT algorithm, one would perform it after every CPT iteration.

If the optics create a divergent beam and the sample dimensions are larger than the depth of focus, the multislice technique [46–51], known from 2D pychography, could also be implemented in this framework. This was already proposed and simulated in multiple publications in different ways [10,52–54]. This implementation deals only with rotations around a single axis, ρ_y . Therefore, phase wedges from the 2D projections, a known artifact of the ePIE algorithm, are suppressed in the $\rho_x - \rho_z$ plane. A global phase wedge in the volume along the ρ_y axis direction can

still arise. Recording additional rotations around the ρ_x axis would suppress these.

An additional object constraint, similar to the one used in coherent x-ray diffraction imaging experiments, could be used in the reconstruction. A mask could be applied to the volume every time it is updated using the information from one projection angle. The mask would enforce everything outside a certain radius to be nonabsorbing and nonphase shifting. This pulls the reconstruction towards a volume where everything outside the sample has an amplitude of 1 and zero phase shift, removing the arbitrary phase offset of the volume and the arbitrary amplitude factor between object and probe. This could prevent the ePIE algorithm from spreading artifacts at the edge of the field of view, such as the bright ring seen in the CPT reconstructions, which surrounds the scanned field of view.

With MAX IV in Lund, Sweden, the first fourth-generation synchrotron light source became operational recently, and many more are to come in the future [55–57]. These storage rings with ultralow emittance offer a larger coherent fraction of the x-ray beam, leading to a significant increase in coherent flux. This boosts coherent imaging techniques such as PXCT. The gain in coherent flux can be used to reduce the total time needed for pychographic tomography experiments, making time-resolved experiments possible. At PETRA IV [57], the future upgrade of PETRA III, a speedup of about 3 orders of magnitude is expected, making it possible to perform the present experiment in about 1 min, rather than 440 min, with the same fluence (dose density). Alternatively, the sample volume could be enlarged more than sevenfold in each dimension and still be imaged in the same time under the same fluence conditions. By increasing the fluence on the sample and recording more rotation angles, higher 3D resolution can be achieved. In the latter case, the sample will have to withstand this higher fluence. Taking advantage of the redundancy in the tomographic data set, the CPT algorithm may be used to fully exploit dose fractionation, allowing us to work with a smaller overall dose on the sample wherever possible. At the very least, the presented algorithm allows for more flexible scanning schemes, as the requirement for each projection to be able to reconstruct on its own is void.

5. CONCLUSION

We have shown that the framework suggested by Gürsoy [9] can be used to reconstruct a 3D object from real experimental pychotomographic data. The predicted relaxation in sampling has been proven correct. The achieved resolution in the reconstructed volume improved with the usage of Algorithm 1 compared to the standard PXCT framework.

Aligning the projections relative to the rotation axis still required a preceding reconstruction of the projections. In the future, this can be avoided with improved mechanical accuracy and stability of the scanning stages. The algorithm used was not optimized for speed, but can be adapted by parallelizing multiple aspects of the algorithm. Nonetheless, the reconstruction of 290 million (660^3) complex variables was performed within seven days on a single machine utilizing 16 CPUs. Including pychographic multislice techniques would allow us to deal with thick samples and strongly diverging probing beams.

Funding. Bundesministerium für Bildung und Forschung (05K16VK1, 5K13WC3).

Acknowledgment. We acknowledge DESY (Hamburg, Germany), a member of the Helmholtz Association HGF, for the provision of experimental facilities. Parts of this research were carried out at beamline P06 of PETRA III. The data were collected during the beamtime (ID 11004381). We would like to thank Mikhail Lyubomirskiy and Andreas Schropp for their help in using the P06 nanoprobe and Satishkumar Kulkarni for the FIB preparation of the sample at DESY NanoLab. The raw data set used for the results presented in this article is openly available via zenodo [58]. All figures/pictures are licensed under CC-BY.

See Supplement 1 for supporting content.

REFERENCES

1. F. Pfeiffer, "X-ray ptychography," *Nat. Photonics* **12**, 9–17 (2018).
2. M. Holler, M. Guizar-Sicairos, E. H. R. Tsai, R. Dinapoli, E. Müller, O. Bunk, J. Raabe, and G. Aeppli, "High-resolution non-destructive three-dimensional imaging of integrated circuits," *Nature* **543**, 402–406 (2017).
3. J. C. da Silva, J. Haubrich, G. Requena, M. Hubert, A. Pacureanu, L. Bloch, Y. Yang, and P. Cloetens, "High energy near- and far-field ptychographic tomography at the ESRF," *Proc. SPIE* **10391**, 1039106 (2017).
4. M. Stockmar, M. Hubert, M. Dierolf, B. Enders, R. Clare, S. Allner, A. Fehrer, I. Zanette, J. Villanova, J. Laurencin, P. Cloetens, F. Pfeiffer, and P. Thibault, "X-ray nanotomography using near-field ptychography," *Opt. Express* **23**, 12720–12731 (2015).
5. Y.-S. Yu, M. Farmand, C. Kim, Y. Liu, C. P. Grey, F. C. Strobridge, T. Tyliczszak, R. Celestre, P. Denes, J. Joseph, H. Krishnan, F. R. N. C. Maia, A. L. D. Kilcoyne, S. Marchesini, T. P. C. Leite, T. Warwick, H. Padmore, J. Cabana, and D. A. Shapiro, "Three-dimensional localization of nanoscale battery reactions using soft x-ray tomography," *Nat. Commun.* **9**, 921 (2018).
6. H. F. Dam, T. R. Andersen, E. B. L. Pedersen, K. T. S. Thydén, M. Helgesen, J. E. Carlé, P. S. Jørgensen, J. Reinhardt, R. R. Søndergaard, M. Jørgensen, E. Bundgaard, F. C. Krebs, and J. W. Andreasen, "Enabling flexible polymer tandem solar cells by 3D ptychographic imaging," *Adv. Energy Mater.* **5**, 1400736 (2015).
7. D. Batey, S. Picipicia, X. Shi, S. Williams, K. Wanelik, A. Wilson, S. Pérez-Tamarit, P. Cimavilla, M. A. Rodríguez-Pérez, and C. Rau, "Coherence branch at I13, DLS: the multiscale, multimodal, ptychographic end station," *Microsc. Microanal.* **24**, 40–41 (2018).
8. S. Sala, D. J. Batey, A. Prakash, S. Ahmed, C. Rau, and P. Thibault, "Ptychographic x-ray computed tomography at a high-brilliance x-ray source," *Opt. Express* **27**, 533–542 (2019).
9. D. Gürsoy, "Direct coupling of tomography and ptychography," *Opt. Lett.* **42**, 3169–3172 (2017).
10. M. A. Gilles, Y. S. G. Nashed, M. Du, C. Jacobsen, and S. M. Wild, "3D x-ray imaging of continuous objects beyond the depth of focus limit," *Optica* **5**, 1078–1086 (2018).
11. S. Aslan, V. Nikitin, D. J. Ching, T. Bicer, S. Leyffer, and D. Gürsoy, "Joint ptycho-tomography reconstruction through alternating direction method of multipliers," *Opt. Express* **27**, 9128–9143 (2019).
12. T. Ramos, B. E. Grønager, M. S. Andersen, and J. W. Andreasen, "Direct three-dimensional tomographic reconstruction and phase retrieval of far-field coherent diffraction patterns," *Phys. Rev. A* **99**, 023801 (2019).
13. P. Thibault, M. Dierolf, O. Bunk, A. Menzel, and F. Pfeiffer, "Probe retrieval in ptychographic coherent diffractive imaging," *Ultramicroscopy* **109**, 338–343 (2009).
14. M. Guizar-Sicairos and J. R. Fienup, "Phase retrieval with transverse translation diversity: a nonlinear optimization approach," *Opt. Express* **16**, 7264–7278 (2008).
15. A. M. Maiden and J. M. Rodenburg, "An improved ptychographical phase retrieval algorithm for diffractive imaging," *Ultramicroscopy* **109**, 1256–1262 (2009).
16. P. Thibault and M. Guizar-Sicairos, "Maximum-likelihood refinement for coherent diffractive imaging," *New J. Phys.* **14**, 063004 (2012).
17. C. G. Schroer, M. Seyrich, M. Kahnt, S. Botta, R. Döhrmann, G. Falkenberg, J. Garrevoet, M. Lyubomirskiy, M. Scholz, A. Schropp, and F. Wittwer, "PtyNAMi: ptychographic nano-analytical microscope at PETRA III—interferometrically tracking positions for 3D x-ray scanning microscopy using a ball-lens retroreflector," *Proc. SPIE* **10389**, 103890E (2017).
18. A. Schropp, R. Hoppe, J. Patommel, D. Samberg, F. Seiboth, S. Stephan, G. Wellenreuther, G. Falkenberg, and C. G. Schroer, "Hard x-ray scanning microscopy with coherent radiation: beyond the resolution of conventional x-ray microscopes," *Appl. Phys. Lett.* **100**, 253112 (2012).
19. J. Reinhardt, R. Hoppe, G. Hofmann, C. D. Damsgaard, J. Patommel, C. Baumbach, S. Baier, A. Rochet, J.-D. Grunwaldt, G. Falkenberg, and C. G. Schroer, "Beamstop-based low-background ptychography to image weakly scattering objects," *Ultramicroscopy* **173**, 52–57 (2017).
20. R. Hoppe, J. Reinhardt, G. Hofmann, J. Patommel, J.-D. Grunwaldt, C. D. Damsgaard, G. Wellenreuther, G. Falkenberg, and C. G. Schroer, "High-resolution chemical imaging of gold nanoparticles using hard x-ray ptychography," *Appl. Phys. Lett.* **102**, 203104 (2013).
21. A. G. Machoke, A. M. Beltrán, A. Inayat, B. Winter, T. Weissenberger, N. Kruse, R. Güttel, E. Spiecker, and W. Schwieger, "Micro/macroporous system: Mfi-type zeolite crystals with embedded macropores," *Adv. Mater.* **27**, 1066–1070 (2015).
22. T. Weissenberger, R. Leonhardt, B. Apeleo Zubiri, M. Pitínová-Šteková, T. L. Sheppard, B. Reiprich, J. Bauer, R. Dotzel, M. Kahnt, A. Schropp, C. G. Schroer, J.-D. Grunwaldt, J. Casci, J. Čejka, E. Spiecker, and W. Schwieger, "Synthesis and characterisation of hierarchically structured titanium silicalite-1 zeolites with large intracrystalline macropores," *Chemistry* **25**, 03287 (2019).
23. M. Guizar-Sicairos, A. Diaz, M. Holler, M. S. Lucas, A. Menzel, R. A. Wepf, and O. Bunk, "Phase tomography from x-ray coherent diffractive imaging projections," *Opt. Express* **19**, 21345–21357 (2011).
24. A. Andersen and A. Kak, "Simultaneous algebraic reconstruction technique (SART): a superior implementation of the ART algorithm," *Ultrason. Imaging* **6**, 81–94 (1984).
25. M. Jiang and G. Wang, "Convergence of the simultaneous algebraic reconstruction technique (SART)," *IEEE Trans. Image Process.* **12**, 957–961 (2003).
26. A. Chambolle, "An algorithm for total variation minimization and applications," *J. Math. Imaging Vis.* **20**, 73–97 (2004).
27. M. Holler, A. Diaz, M. Guizar-Sicairos, P. Karvinen, E. Färm, E. Härkönen, M. Ritala, A. Menzel, J. Raabe, and O. Bunk, "X-ray ptychographic computed tomography at 16 nm isotropic 3D resolution," *Sci. Rep.* **4**, 3857 (2014).
28. M. Guizar-Sicairos, I. Johnson, A. Diaz, M. Holler, P. Karvinen, H.-C. Stadler, R. Dinapoli, O. Bunk, and A. Menzel, "High-throughput ptychography using Eiger: scanning x-ray nano-imaging of extended regions," *Opt. Express* **22**, 14859–14870 (2014).
29. M. Soleimani and T. Pengpen, "Introduction: a brief overview of iterative algorithms in x-ray computed tomography," *Philos. Trans. A Math. Phys. Eng. Sci.* **373**, 20140399 (2015).
30. C. Badea and R. Gordon, "Experiments with the nonlinear and chaotic behaviour of the multiplicative algebraic reconstruction technique (MART) algorithm for computed tomography," *Phys. Med. Biol.* **49**, 1455 (2004).
31. T. Gerzen and D. Minkwitz, "Simultaneous multiplicative column-normalized method (SMART) for 3-D ionosphere tomography in comparison to other algebraic methods," *Ann. Geophys.* **34**, 97–115 (2016).
32. R. Gordon, R. Bender, and G. T. Herman, "Algebraic reconstruction techniques (ART) for three-dimensional electron microscopy and x-ray photography," *J. Theor. Biol.* **29**, 471–481 (1970).
33. P. Gilbert, "Iterative methods for the three-dimensional reconstruction of an object from projections," *J. Theor. Biol.* **36**, 105–117 (1972).
34. Y. S. G. Nashed, D. J. Vine, T. Peterka, J. Deng, R. Ross, and C. Jacobsen, "Parallel ptychographic reconstruction," *Opt. Express* **22**, 32082–32097 (2014).
35. S. Marchesini, H. Krishnan, B. J. Daurer, D. A. Shapiro, T. Perciano, J. A. Sethian, and F. R. N. C. Maia, "SHARP: a distributed GPU-based ptychographic solver," *J. Appl. Crystallogr.* **49**, 1245–1252 (2016).
36. P. Thibault and A. Menzel, "Reconstructing state mixtures from diffraction measurements," *Nature* **494**, 68–71 (2013).
37. F. Wittwer, R. Hoppe, F. Seiboth, J. Reinhardt, M. Scholz, and C. G. Schroer, "Ptychography with a virtually enlarged illumination," *Microsc. Microanal.* **24**, 46–47 (2018).
38. A. Schropp, R. Hoppe, V. Meier, J. Patommel, F. Seiboth, H. J. Lee, B. Nagler, E. C. Galtier, B. Arnold, U. Zastrau, J. B. Hastings, D. Nilsson, F. Uhlén, U. Vogt, H. M. Hertz, and C. G. Schroer, "Full spatial

- characterization of a nanofocused x-ray free-electron laser beam by ptychographic imaging," *Sci. Rep.* **3**, 1633 (2013).
39. F. Zhang, I. Peterson, J. Vila-Comamala, A. Diaz, F. Berenguer, R. Bean, B. Chen, A. Menzel, I. K. Robinson, and J. M. Rodenburg, "Translation position determination in ptychographic coherent diffraction imaging," *Opt. Express* **21**, 13592–13606 (2013).
 40. P. M. Pelz, M. Guizar-Sicairos, P. Thibault, I. Johnson, M. Holler, and A. Menzel, "On-the-fly scans for x-ray ptychography," *Appl. Phys. Lett.* **105**, 251101 (2014).
 41. J. Deng, Y. S. G. Nashed, S. Chen, N. W. Phillips, T. Peterka, R. Ross, S. Vogt, C. Jacobsen, and D. J. Vine, "Continuous motion scan ptychography: characterization for increased speed in coherent x-ray imaging," *Opt. Express* **23**, 5438–5451 (2015).
 42. X. Huang, K. Lauer, J. N. Clark, W. Xu, E. Nazaretski, R. Harder, I. K. Robinson, and Y. S. Chu, "Fly-scan ptychography," *Sci. Rep.* **5**, 9074 (2015).
 43. M. Odstrčil, M. Holler, and M. Guizar-Sicairos, "Arbitrary-path fly-scan ptychography," *Opt. Express* **26**, 12585–12593 (2018).
 44. B. Enders, M. Dierolf, P. Cloetens, M. Stockmar, F. Pfeiffer, and P. Thibault, "Ptychography with broad-bandwidth radiation," *Appl. Phys. Lett.* **104**, 171104 (2014).
 45. D. J. Batey, D. Claus, and J. M. Rodenburg, "Information multiplexing in ptychography," *Ultramicroscopy* **138**, 13–21 (2014).
 46. A. M. Maiden, M. J. Humphry, and J. M. Rodenburg, "Ptychographic transmission microscopy in three dimensions using a multi-slice approach," *J. Opt. Soc. Am. A* **29**, 1606–1614 (2012).
 47. T. M. Godden, R. Suman, M. J. Humphry, J. M. Rodenburg, and A. M. Maiden, "Ptychographic microscope for three-dimensional imaging," *Opt. Express* **22**, 12513–12523 (2014).
 48. A. Suzuki, S. Furutaku, K. Shimomura, K. Yamauchi, Y. Kohmura, T. Ishikawa, and Y. Takahashi, "High-resolution multislice x-ray ptychography of extended thick objects," *Phys. Rev. Lett.* **112**, 053903 (2014).
 49. E. H. R. Tsai, I. Usov, A. Diaz, A. Menzel, and M. Guizar-Sicairos, "X-ray ptychography with extended depth of field," *Opt. Express* **24**, 29089–29108 (2016).
 50. H. Öztürk, H. Yan, Y. He, M. Ge, Z. Dong, M. Lin, E. Nazaretski, I. K. Robinson, Y. S. Chu, and X. Huang, "Multi-slice ptychography with large numerical aperture multilayer Laue lenses," *Optica* **5**, 601–607 (2018).
 51. X. Huang, H. Yan, Y. He, M. Ge, H. Öztürk, Y.-L. L. Fang, S. Ha, M. Lin, M. Lu, E. Nazaretski, I. K. Robinson, and Y. S. Chu, "Resolving 500 nm axial separation by multi-slice X-ray ptychography," *Acta Crystallogr. A* **75**, 336–341 (2019).
 52. P. Li and A. Maiden, "Multi-slice ptychographic tomography," *Sci. Rep.* **8**, 2049 (2018).
 53. K. Shimomura, M. Hirose, T. Higashino, and Y. Takahashi, "Three-dimensional iterative multislice reconstruction for ptychographic x-ray computed tomography," *Opt. Express* **26**, 31199–31208 (2018).
 54. E. H. R. Tsai, F. Marone, and M. Guizar-Sicairos, "Gridrec-ms: an algorithm for multi-slice tomography," *Opt. Lett.* **44**, 2181–2184 (2019).
 55. P. F. Tavares, E. Al-Dmour, Å. Andersson, F. Cullinan, B. N. Jensen, D. Olsson, D. K. Olsson, M. Sjöström, H. Tarawneh, S. Thorin, and A. Vorozhtsov, "Commissioning and first-year operational results of the MAX IV 3 GeV ring," *J. Synchrotron Rad.* **25**, 1291–1316 (2018).
 56. P. Raimondi, "ESRF-EBS: the extremely brilliant source project," *Synchr. Rad. News* **29**(6), 8–15 (2016).
 57. C. G. Schroer, I. Agapov, W. Brefeld, R. Brinkmann, Y.-C. Chae, H.-C. Chao, M. Eriksson, J. Keil, X. N. Gavalda, R. Röhlberger, O. H. Seeck, M. Sprung, M. Tischer, R. Wanzenberg, and E. Weckert, "PETRA IV: the ultra-low emittance source project at DESY," *J. Synchrotron Rad.* **25**, 1277–1290 (2018).
 58. M. Kahnt, J. Becher, D. Brückner, Y. Fam, T. Sheppard, F. Weissenberger, J.-D. Wittwer, J.-D. Grunwaldt, W. Schwieger, and C. G. Schroer, "Raw data for 'Coupled ptychography and tomography algorithm improves reconstruction of experimental data,'" [Data set], Zenodo, <https://doi.org/10.5281/zenodo.3402977>.